Drying creep of concrete: constitutive model and new experiments separating its mechanisms

ZDENĚK P. BAŽANT, YUNPING XI

Department of Civil Engineering, Northwestern University, Evanston, IL 60208, USA

A new experimental method which allows the direct separation of the components of drying creep due to microcracking and stress-induced shrinkage is developed, demonstrated and validated. The basic idea is to compare the curvature creep of beams subjected to the same bending moment but very different axial forces. The results confirm that drying creep has two different sources: microcracking and stress-induced shrinkage. The latter increases continuously, whereas the former first increases and then decreases. The test results are fitted using a finite element model. The results validate the present model for drying creep. The microcracking is described by an established model, and the free (unrestrained) shrinkage of a material element is shown to depend approximately linearly on the humidity drop.

1. INTRODUCTION

The Pickett effect [1], also called drying creep, is the excess of creep at drying over the sum of shrinkage and basic creep, as shown in Fig. 1. Over the last 50 years, several hypotheses have been presented to explain the mechanisms of this effect [1–8, 32].

Most of the models have tried to explain the excess deformation by the so-called microcracking effect. Because of the non-uniformity of moisture distribution in a shrinkage specimen (specimen No. 1, Fig. 1), the surface layer of the specimen dries and shrinks first, while the inner layer remains wet and does not shrink. As a result, the surface layer is in tension while the inner layer is in compression at the initial stage of the drying process. The tensile stress causes local microcracking or tensile strain-softening in the surface layer, which has been investigated by many authors [2, 9–13]. Due to the

Central loading

$$\Delta\varepsilon_{sh} + \Delta\varepsilon_{bc} < \Delta\varepsilon_{dc}$$ Pickett effect in centric loading

Fig. 1 Pickett effect in centric loading.

nonlinear inelastic behaviour and unrecoverable creep of concrete caused by the tensile stress, the microcracks cannot close fully when the moisture distribution finally approaches a uniform state. As a result, the measured shrinkage of the specimen is always smaller than the true shrinkage of the specimen. It is this irreversible deformation that reduces the total shrinkage of the specimen. On the other hand, for drying creep specimens (specimen No. 3, Fig. 1), the whole cross-section is in compression, and thus there is no microcracking on the planes normal to the direction of compression. So the observed specimen shrinkage does not get reduced by microcracking and the related irreversible deformations. This means that the drying creep must be larger than the sum of the separately observed basic creep and shrinkage.

Partly differing from the others, Bažant and Chern [6, 7] pointed out that microcracking (or tensile strain-softening) and other irreversible strains form only a part of the Pickett effect. Another mechanism exists: stress-induced shrinkage. This mechanism may be explained from a different point of view. Basically, two different types of moisture diffusion process can be distinguished: macrodiffusion (drying and wetting) and microdiffusion. Microdiffusion transports water locally between the capillary pores (macropores) and gel pores (micropores), and this transport affects the deformation rate of the solid framework of cement gel. The movement of water molecules through the gel pores promotes the breakage of bonds which are the source of creep, and thus influences creep [14, 15].

However, there are no experimental data currently in the literature that distinguish clearly among the proposed mechanisms. The occurrence of the latter mechanism has been shown previously rather indirectly by a complete computer analysis of various results of tests [6, 7], and was implied indirectly in the thermodynamic analysis by Bažant [14, 15]. The conventional creep test with centric loading and the bending creep test can show only the
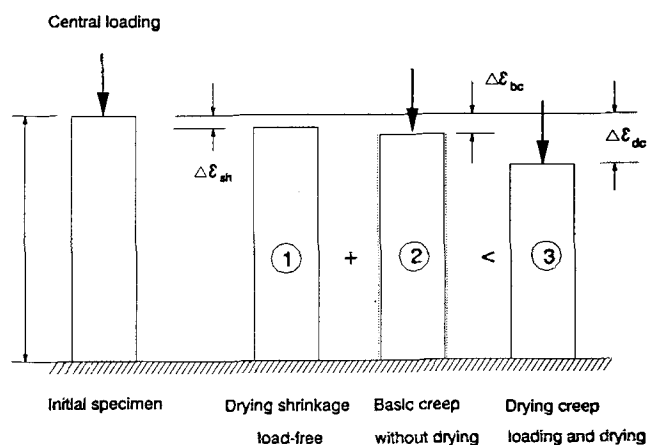
Pickett effect itself, but cannot detect the different mechanisms involved. The first objective of this paper is to present a drying creep experiment which directly distinguishes the aforementioned mechanisms and provides a clear experimental basis for establishing the correct theoretical model. The basic idea of this experiment was presented in 1989 [16], and preliminary reports on the test results were made at two recent conferences [17, 18].

Many mathematical models with diverse mechanism concepts have been proposed for creep, shrinkage, and drying creep of concrete (for review see [19] chap. 2). Among them, Bažant and Chern's model [6–8] has been the only one that attempts to describe both of the aforementioned mechanisms of drying creep. At the time of those studies, however, some aspects were not understood as well as now: for example, the solidification aspect of basic creep and certain consequences of the diffusion theory for shrinkage. Furthermore, the parameters of the model could not have been calibrated accurately due to the absence of experiments that clearly separate the effect of each mechanism.

The second objective of this paper is to establish an experimentally well supported theoretical model for drying creep. For basic creep, the recently developed continuous retardation spectrum will be used to characterize the non-ageing creep component [20], and then the solidification concept [21, 22] will be applied to introduce the ageing aspect of creep. For shrinkage, a new local constitutive relation for relative humidity and shrinkage strain will be formulated, based on recent test results. For stress-induced shrinkage, the microdiffusion concept of Bažant and Chern [6] will be retained, but the mathematical formulation will be refined and modified. For the microcracking effect, a model that has been used for other similar types of softening behaviour of concrete will be employed. Finally, the parameters of the model will be calibrated by new test results.

2. NEW EXPERIMENTS TO SEPARATE VARIOUS MECHANISMS

2.1 Basic idea

The basic idea is to measure the curvature creep of specimens subjected to the same bending moment but very different axial forces. The advantage of measuring curvature creep is that shrinkage does not contaminate the results because it causes no curvature in a symmetric and symmetrically drying specimen (it is assumed that the stresses and microcracking do not affect the water diffusion significantly).

The desired loadings are axial loads with different eccentricities. Fig. 2 shows type 1 and type 2 specimens with small eccentricity, and Fig. 3 shows type 3 and type 4 specimens with large eccentricity. Type 1 and type 3 specimens are for basic creep, and are therefore sealed on all four sides, whereas type 2 and type 4 specimens
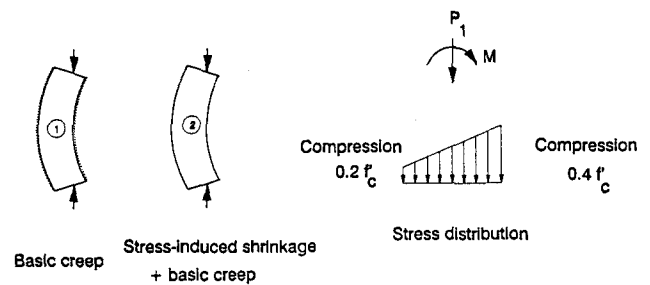

Fig. 2 Experimental plan for small eccentricity of loading.

are for drying creep and are sealed on two sides (and the ends) to make the moisture diffusion process one-dimensional.

The load magnitudes and eccentricities are chosen so that the bending moments for the two loading cases are exactly the same. Consequently, the deformations due to the two different mechanisms of drying creep can be separated by measuring curvatures.

First, when specimens with small eccentricity are loaded, the whole cross-section is in compression (Fig. 2), which eliminates the tensile microcracking effect. Thus, deformation of the type 1 specimen is due solely to basic creep. Therefore, if any excess deformation is observed on the type 2 specimen, it means that stress-induced shrinkage exists and contributes to the drying creep. Second, when the specimens with large eccentricity are loaded, there is both tension and compression in the cross-section. Deformation of the type 3 specimen (see Fig. 3) is from basic creep only. The irreversible deformation, particularly microcracking, causes excess deformation in the tensile region of the cross-section of the type 4 specimen, and thus extra curvature. Hence, any extra curvature in the type 4 specimen compared with the type 2 represents deformation due to microcracking. This is the basic idea of the present experimental approach.

Keeping the stresses within the service stress range, one can treat the creep as approximately linear. Thus, the bending curvatures observed can be characterized in terms of the compliance function $J(t, t')$. This function can then be decomposed into the terms corresponding to the two different mechanisms.
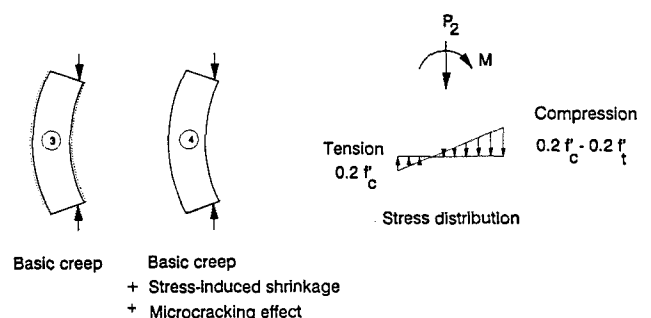

Fig. 3 Experimental plan for large eccentricity of loading.

2.2 Experimental procedure

The experimental setup, shown in Fig. 4, was the standard setup recommended by ASTM. The specimens were square prisms of length 16 in (40.64 cm) and side 4 in (10.16 cm). For eccentric loading, a one-way hinge at the top of the specimens and a two-way hinge at the bottom were used. In this way, the load axis could be kept at the centre of the cross-section in one horizontal direction and off-centre in the perpendicular horizontal direction.

Lateral deflections were measured on both sides during the test, and then averaged. Each time, before taking a reading, the load was adjusted to a constant load value. The experiments were carried out in a moisture room. The environmental relative humidity was controlled at 50%, and the temperature was held constant at 80°F (26.7°C).

Two sets of tests have been carried out. In set I, there were two different eccentricities, small and large, and two different moisture conditions, drying and sealed. For each loading and moisture condition, there were two identical specimens, with a total of eight specimens in set I. The lateral deflection measured in set I was designed to be used to verify different mechanisms. Therefore, all specimens in set I were subjected to the same bending moment and were cast from the same batch of concrete.

Set II involved four specimens cast from another batch. There were two moisture conditions but only one eccentricity – small. For each loading and moisture condition two identical specimens were cast. To check the drying creep mechanisms at different loading levels, the bending moment in set II was designed to be different from that in set I. Further information on the two sets is listed in Table 1.

All the specimens used in the two sets were cast identically, in a horizontal position, and cured identically. The
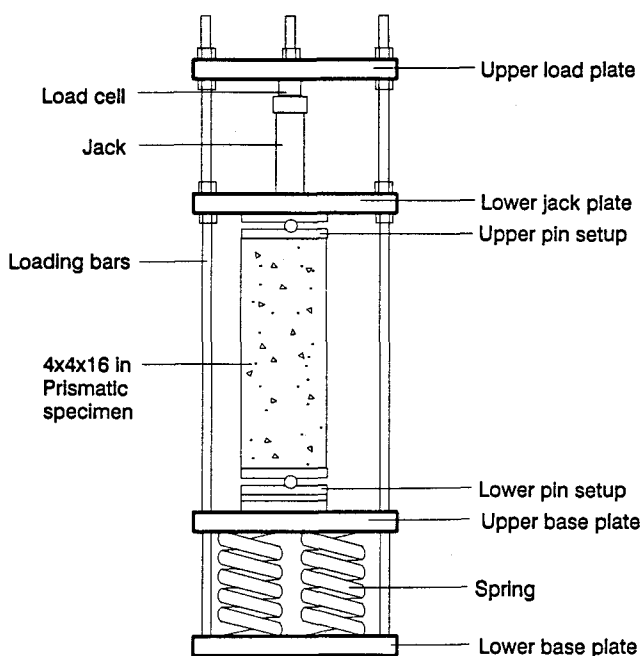
Table 1 Basic data on the experiments

	Set I		Set II
	Small e_0	Large e_0	Small e_0
e_0 (in)	0.21	0.97	0.44
No. spec.	4	4	4
f'_c (psi)	5 619	5 619	5 418
Size (in)	$4 \times 4 \times 16$	$4 \times 4 \times 16$	$4 \times 4 \times 16$
P (lb)	26 971	6 112	26 006
σ_{max} (psi)	2 248	944	2 847
σ_{min} (psi)	1 124	-180	403

mix ratios were water:cement:sand:gravel = 0.5:1.0:2.5:3.0 (by weight). Type I cement was used. The aggregate was crushed limestone with a maximum size of 3/4 in (1.9 cm). The forms were removed after one day of moist curing at room temperature, and the sides of each specimen were sealed with siliconized acrylic latex caulk.

2.3. Test results and discussions

Fig. 5 shows the averages of the lateral deflections for each pair of identical specimens. First, by comparing the deflections of the sealed and unsealed specimens with the small eccentricity (solid squares), it is noticeable that there is an additional deformation, added to basic creep. Since, with small eccentricities, the whole cross-section is in compression, microcracking cannot occur. So the additional deformation that is seen in Fig. 5 must come from the stress-induced shrinkage. This is a direct experimental proof of the existence of stress-induced shrinkage.

Furthermore, comparing the sealed and unsealed specimens with large eccentricity (the circles in Fig. 5). it is seen that there is also an additional deformation, added to basic creep. This extra deformation combines the contributions from the two mechanisms, microcracking and stress-induced shrinkage.

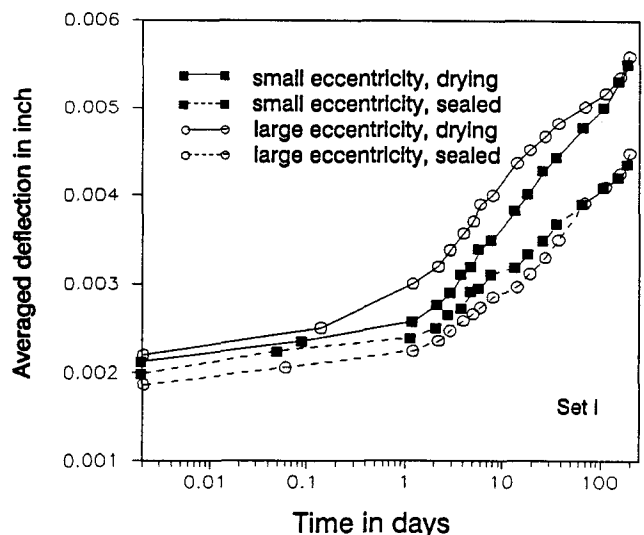Fig. 4 Experimental setup for eccentric loading.

Fig. 5 Averaged deflections.

The deflection magnitude depends on many parameters, such as the prism length, cross-section size, and eccentricity. To compare test results, the compliance function can be employed. The compliance function J can be calculated easily from the measured mid-span lateral deflection y_{max}. According to the theory of elastic buckling [23], chap. 1),

$$J = \frac{1}{E} = \frac{I}{P}\left[\frac{2}{l}\arccos\left(\frac{e_0}{y_{max} + e_0}\right)\right]^2, \qquad (1)$$

where I is the centroidal inertia moment of the cross-section, P is the axial load, l is the length of the column, and e_0 is the initial eccentricity. For small P and small y_{max}, Equation 1 may be approximated as

$$J = \frac{1}{E} = \frac{8I}{l^2 P e_0} y_{max}. \qquad (2)$$

This eliminates from the creep observations the effects of P, e_0, l, and I. Therefore, the test results for different loading moments, column lengths, and cross-sections can be compared with each other in terms of J. This is exactly the same as in the analysis of centric loading tests. In that case, the axial strain ε_1 is measured during the test. Instead of ε_1, the compliance function $J = \varepsilon_1 A/P$ (A is the area of the cross-section) is analysed to get rid of the effects of A and P.

The averaged compliance function, computed from Equation 1, is shown in Fig. 6. One can see that, for identical specimens, loading and moisture conditions, the analysis of compliance function is equivalent to the analysis of lateral deflection and will give the same conclusions as in Fig. 5.

The different mechanisms shown in Fig. 6 can be decomposed as shown in Fig. 7. It is evident that the stress-induced shrinkage increases with time. The microcracking effect can be decomposed further, as shown in Fig. 8. It appears that the microcracking effect increases from the very beginning, reaches its maximum (for this cross-section size) in about 10 days, and then
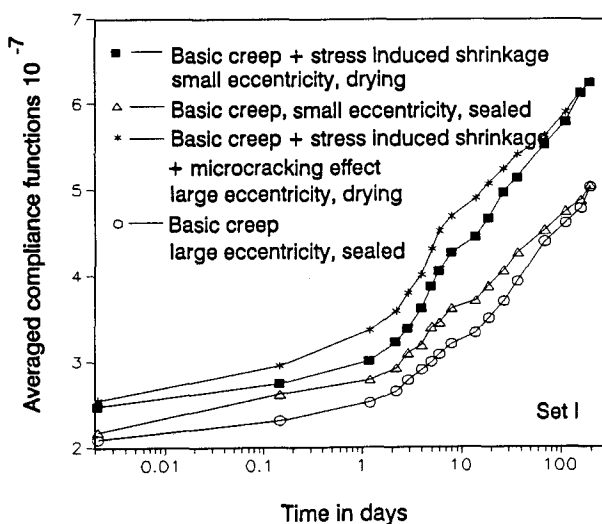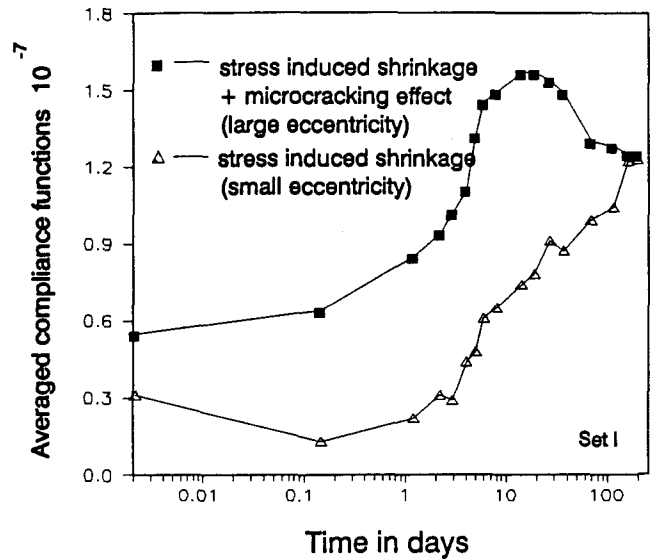

Fig. 7 Decomposition of different drying creep mechanisms.

decreases. This is because moisture distribution gradually approaches a uniform state. However, even after a long time, the microcracks that have developed in the early drying process close only partly, which must be explained by irreversibility of the crack openings.

Fig. 9 shows the averaged compliance function obtained from the results of set II. Comparison with Fig. 6 shows clearly that there is also another deformation, added to the basic creep. Since the whole cross-section is also in compression for set II, there is no microcracking effect. The observed additional deformation must come from the mechanism of stress-induced shrinkage. Noting that the bending moments and axial loads in sets II and I are different, we further conclude that the drying creep mechanisms, distinguished from each other by the experiment in set I, truly occur for various loading levels.
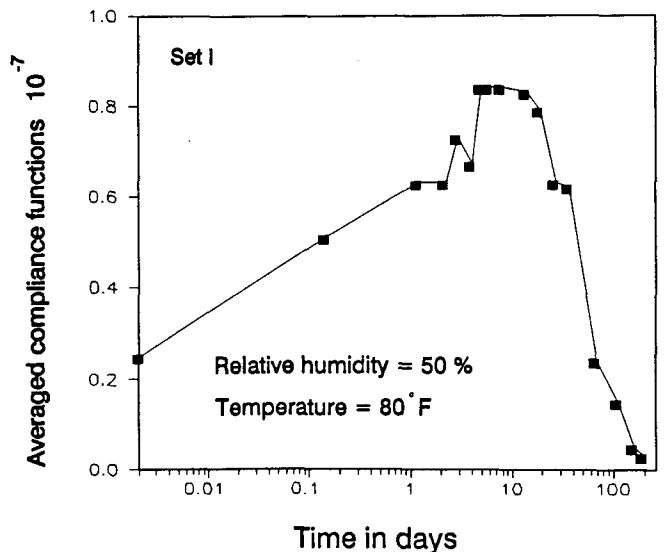

Fig. 6 Averaged compliance function.

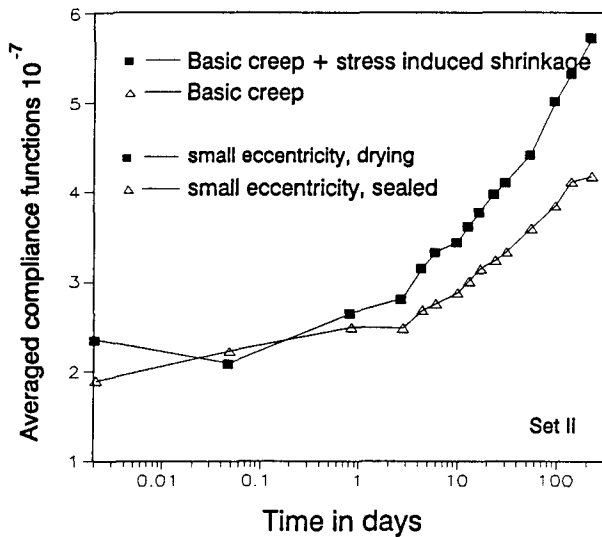Fig. 8 Effect of microcracking on drying creep.

Fig. 9 Averaged compliance functions of set II.

3. CONSTITUTIVE MODEL

3.1 Review of basic creep model with ageing

The ageing aspect of creep is handled by solidification theory. The key feature of the theory (Fig. 10) is that the ageing aspect of concrete creep is considered to be caused by the growth of the volume fraction $v(t)$ of the effective load-bearing portion of solidified matter (i.e., hydrated cement), representing an increase of both the volume fraction of the hydrated cement and the load-bearing solid fraction, which is growing due to the formation of further bonds (or polymerization of calcium silicate hydrates). The principal advantage is that, in this theory, the properties of all the constituents, including the load-bearing matter, are age-independent (as required by thermodynamics). This makes it possible to apply the conventional theory of non-ageing viscoelasticity. The creep strain rate $\dot{\varepsilon}^v$, corresponding to the solid part, can be expressed as the product of the age-independent strain rate of solid $\dot{\gamma}$, and the increase of the volume

fraction $v(t)$ of the solid [21, 22]:

$$\dot{\varepsilon}^v(t) = \frac{F[\sigma(t)]}{v(t)} \dot{\gamma}(t), \tag{3}$$

where function $F[\sigma(t)]$ is introduced to reflect nonlinear behaviour at high stress (at low stress, $F[\sigma(t)] = 1$).

In this formulation, all of the procedures developed for non-ageing basic creep are applicable to the visco-elastic microstrain γ^v. Applying the well-known Kelvin chain model with N Kelvin units, we then have, for a constant uniaxial stress σ [20],

$$\gamma^v = \left[\sum_{\mu=1}^{N} A_\mu (1 - e^{-\xi/\tau_\mu}) \right] \sigma \tag{4}$$

where ξ is the load duration. Analogously to Equation 3, we have for the flow term:

$$\dot{\varepsilon}^f(t) = q_3 \frac{F[\sigma(t)]}{v(t)} \sigma(t), \tag{5}$$

where q_3 is an empirical coefficient which depends on the composition of concrete.

One important advantage of the solidification theory is that, when the age-independent creep strain γ is modelled by a generalized Kelvin chain, A_μ in Equation 4 can be determined [20] by the method of continuous retardation spectrum $L(\tau_\mu)$. If τ_μ is known, then, approximately (but with very good accuracy)

$$A_\mu = L(\tau_\mu) \ln(10) \Delta(\log \tau_\mu), \tag{6}$$

where $\Delta(\log \tau_\mu)$ is the time interval between the retardation times of two adjacent Kelvin units in the logarithmic time scale. Computational experience shows that the choice $\Delta(\log \tau_\mu) = \log 10 = 1$ gives a sufficiently smooth compliance function, while greater separations of τ_μ give a bumpy appearance to the creep curves. $L(\tau_\mu)$ depends on the compliance function of the concrete. For the compliance function of the non-ageing constituent, we may assume the log-power creep law:

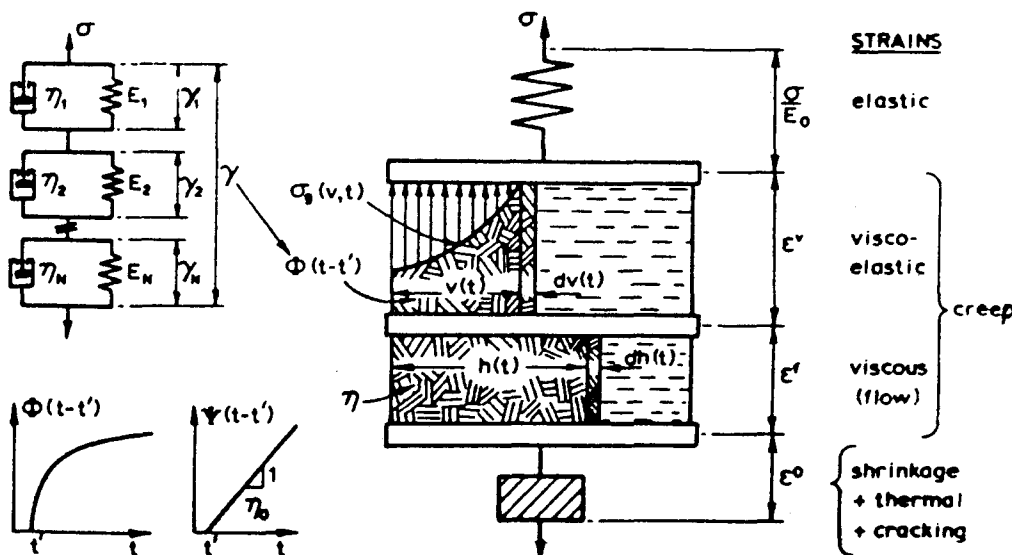$$J(\xi) = q_2 \ln\left[1 + \left(\frac{\xi}{\lambda_0} \right)^n \right] \tag{7}$$

Fig. 10 Solidification theory for basic creep.

in which $\lambda_0 = 1$ day; and q_2 is a parameter depending on the concrete composition.

The method for obtaining A_μ, analogously to the method used in classical non-ageing viscoelasticity, has been presented by Bažant and Xi [20] and will now be outlined briefly. For Equation 7, it has been shown that

$$L(\tau) = \left[\frac{-2n^2(3\tau)^{2n-3}[n-1-(3\tau)^n]}{[1+(3\tau)^n]^3} \right.$$

$$\left. + \frac{n(n-2)(3\tau)^{n-3}[n-1-(3\tau)^n] - n^2(3\tau)^{2n-3}}{[1+(3\tau)^n]^2} \right]$$

$$\times \frac{q_2(3\tau)^3}{2}. \qquad (8)$$

This is the approximate retardation spectrum of order 3. According to the fitting of test data by Bažant and Prasannan [21, 22], n is approximately a constant. In the case of small n, the terms with n^3 in Equation 8 may be neglected without much loss of accuracy. Combining this with some other simplifications of Equation 8, the following expression for the retardation spectrum can be obtained:

$$L(\tau) = q_2 n(1-n) \frac{(3\tau)^n}{1+(3\tau)^n} \qquad (9)$$

Because of its simple form, Equation 9 is attractive as means of creep characterization that could be used in a design code. For computational analysis, such as finite element analysis, or when n is large ($n > 0.45$), Equation 8 ought to be used. To analyse the present tests, eight units of Kelvin chain have been used. To be able to cover the test range by a minimum number of Kelvin units, τ_μ are spaced by decades in $\log \tau_\mu$, i.e., $\tau_1 = 10^{-3}$ and $\tau_{\mu+1} = 10\tau_\mu$, $\mu = 1, 2, \ldots$; A_0 depends on n as given by Table 2, and $\tau_0 = 10^{-7}$; A_μ is given by Equation 6. The rate-type formulation used in finite element analysis is presented in detail by Bažant and Xi [20] and is in principle the same as given by Bažant and Prasannan [21, 22].

3.2 Shrinkage model: relation of local shrinkage to relative humidity

In the idealized case of free shrinkage, in which there is no restraint and no stress and the whole specimen shrinks uniformly, the rate of local shrinkage strain is [6-8]

$$\dot{\varepsilon}_{sh} = k_{sh} \dot{H} \qquad (10)$$

$$k_{sh} = -\varepsilon_s^0 g_s(t) \frac{\mathrm{d}f_s(H)}{\mathrm{d}H} \qquad (11)$$

where k_{sh} is the shrinkage coefficient; ε_s^0 is the ultimate shrinkage, $g_s(t) = E(t_0)/E(t)$, and $E(t)$ can be estimated by

$$E(t) = E(28)\sqrt{\frac{t}{4 + 0.85t}}$$

with

$$E(28) = 33w^{1.5}\sqrt{f_c'} \qquad (12)$$

Table 2 Values of n and A_0

n	A_0	n	A_0
0.004 95	122.732 00	0.232 65	7.968 00
0.009 90	61.984 00	0.237 60	8.026 00
0.014 85	41.780 00	0.242 55	8.085 00
0.019 80	31.713 00	0.247 50	8.145 00
0.024 75	25.701 00	0.252 45	8.207 00
0.029 70	21.717 00	0.257 40	8.268 00
0.034 65	18.893 00	0.262 35	8.329 00
0.039 60	16.794 00	0.267 30	8.390 00
0.044 55	15.179 00	0.272 25	8.450 00
0.049 50	13.903 00	0.277 20	8.508 00
0.054 45	12.874 00	0.282 15	8.563 00
0.059 40	12.031 00	0.287 10	8.617 00
0.064 35	11.331 00	0.292 05	8.667 00
0.069 30	10.743 00	0.297 00	8.712 00
0.074 25	10.245 00	0.301 95	8.754 00
0.079 20	9.822 00	0.306 90	8.789 00
0.084 15	9.459 00	0.311 85	8.819 00
0.089 10	9.147 00	0.316 80	8.841 00
0.094 05	8.879 00	0.321 75	8.855 00
0.099 00	8.647 00	0.326 70	8.860 00
0.103 95	8.447 00	0.331 65	8.855 00
0.108 90	8.275 00	0.336 60	8.838 00
0.113 85	8.127 00	0.341 55	8.808 00
0.118 80	8.000 00	0.346 50	8.764 00
0.123 75	7.892 00	0.351 45	8.704 00
0.128 70	7.801 00	0.356 40	8.627 00
0.133 65	7.726 00	0.361 35	8.530 00
0.138 60	7.664 00	0.366 30	8.412 00
0.143 55	7.614 00	0.371 25	8.271 00
0.148 50	7.575 00	0.376 20	8.104 00
0.153 45	7.547 00	0.381 15	7.909 00
0.158 40	7.528 00	0.386 10	7.682 00
0.163 35	7.518 00	0.391 05	7.422 00
0.168 30	7.515 00	0.396 00	7.125 00
0.173 25	7.520 00	0.400 95	6.788 00
0.178 20	7.531 00	0.405 90	6.406 00
0.183 15	7.549 00	0.410 85	5.976 00
0.188 10	7.572 00	0.415 80	5.493 00
0.193 05	7.601 00	0.420 75	4.953 00
0.198 00	7.634 00	0.425 70	4.351 00
0.202 95	7.671 00	0.430 65	3.680 00
0.207 90	7.713 00	0.435 60	2.934 00
0.212 85	7.758 00	0.440 55	2.108 00
0.217 80	7.806 00	0.445 50	1.194 00
0.222 75	7.858 00	0.450 45	0.184 00
0.227 70	7.912 00	0.455 40	0.001 00

where w is the unit weight of concrete in lb ft^{-3}, and f_c' and E are in psi. For $t \to \infty$, $g_s(t) \to 1$.

Now the important question is the meaning of $f_s(H)$. This is a complicated problem because, until now, there have been no experimental results to identify clearly the function $f_s(H)$. As an approximation, the following equation has been used [19]:

$$f_s(H) = 1 - H^3 \qquad (13)$$

It was obtained by fitting a large amount of test data on shrinkage deformations averaged over the whole
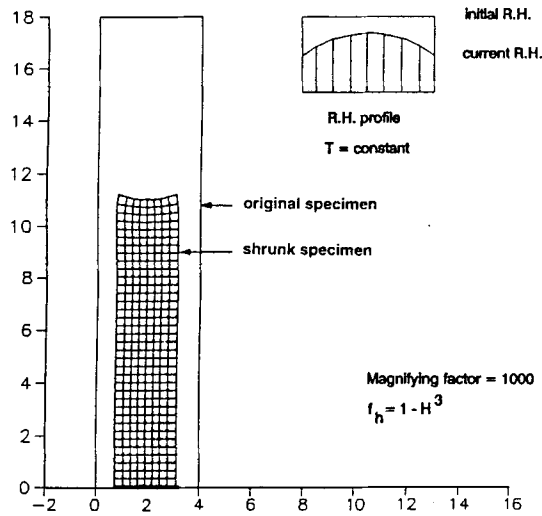
Fig. 11 Shrinkage with previous constitutive relation.

Fig. 12 Shrinkage with linear constitutive relation.

cross-section for different ambient relative humidities [24], and was intended only for such deformations which include the effects of distributed cracking, and creep caused by shrinkage stresses. As a local constitutive relation for a material point, however, Equation 13 does not give best results.

Fig. 11 shows finite element results for the shrinkage strain according to Equation 13. The humidity profile (Fig. 11, upper right) indicates that the outside layer of the specimen has a larger humidity drop. However, calculations based on Equation 13 indicate that the inner layer could shrink more than the outside layer, which is not correct.

Another function, however, is suggested by noting that shrinkage of small specimens has been found to be proportional to the water loss Δw, and according to the desorption isotherms, Δw is often approximately proportional to the humidity drop. According to this argument, we will use

$$f_s(H) = 1 - H.\qquad(14)$$

Indeed, good finite element results for shrinkage have been obtained with this relation (see Fig. 12). By substituting Equation 14 into 11 and then into 10, we obtain

$$\Delta\varepsilon_{sh} = k_{sh}\,\Delta H,\qquad k_{sh} = \varepsilon_s^0 g_s(t)\qquad(15)$$

ε_s^0 in Equation 15 is a material constant representing the magnitude of the final shrinkage value. It is left as a free empirical constant in our model, because of the difficulties in measuring ε_s^0 directly.

3.3 Formulation for stress-induced shrinkage

The Kelvin and Maxwell chains can both approximate linear creep behaviour with any desired accuracy [19]. For the sake of a theoretical argument, it is now simpler to use (temporarily) the Maxwell chain to analyse the stress-induced shrinkage. The same result could be obtained using the Kelvin model, but the derivation
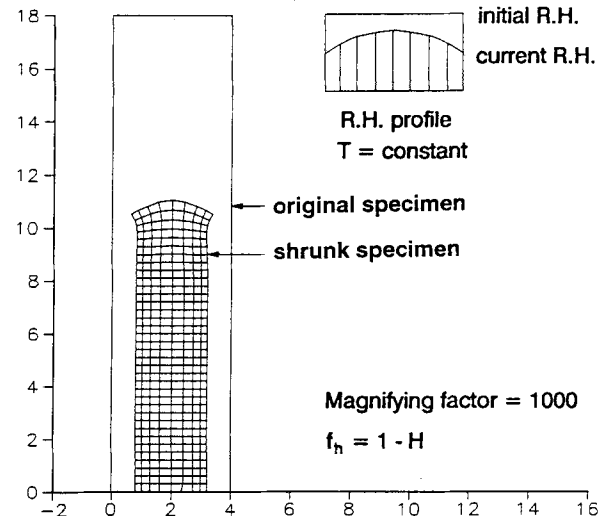
would be less clear because the Kelvin units involve not only the strain rate but also the strain itself. The equation for a single Maxwell unit is

$$\frac{\dot\sigma}{E} + \frac{\sigma}{\bar\eta} = \dot\varepsilon - \dot\varepsilon_{sh} - \dot\varepsilon_T\qquad(16)$$

where $\bar\eta$ is the dashpot viscosity; $\dot\varepsilon_{sh}$ and $\dot\varepsilon_T$ are the shrinkage strain rate and thermal strain rate; and $\dot\varepsilon_T = a_T \dot T$, where a_T = coefficient of thermal expansion.

Because microdiffusion of pore water may be expected to enhance the debonding and rebonding process in cement gel that is the source of creep, the viscosity $\bar\eta$ should be a function of the microdiffusion flux $\bar H$ of water which is driven by a difference in the chemical potential between the capillary water and the gel pore water. At variable temperature T, this difference, in turn, is proportional (as shown by Bažant and Chern [6, 7] to effective pore humidity

$$\bar H = a_1\dot H + a_2\dot T\qquad(17)$$

in which a_1 and a_2 are constants. Note that (1) the microdiffusion flux increases creep and thus decreases viscosity $\bar\eta$, and (2) only the absolute value of $\bar H$ matters since the creep increases regardless of whether the microdiffusion of water goes into or out of the capillary pores. Thus, as a first-order approximation,

$$\frac{1}{\bar\eta} = \frac{1}{\eta} + k'|\bar H|\qquad(18)$$

where η is the viscosity with no microdiffusion, and k' is a constant. Substituting Equations 17 and 18 into 16,

$$\frac{\dot\sigma}{E} + \frac{\sigma}{\eta} = \dot\varepsilon - k\dot H - \bar\alpha\dot T\qquad(19)$$

where

$$k = k_{sh}(1 + r\sigma\,\text{sign}(\bar H))\qquad(20)$$

$$\bar\alpha = a_T(1 + \rho\sigma\,\text{sign}(\bar H))\qquad(21)$$

where $r = k'a_1/k_{sh}$, $\rho = k'a_2/a_T$, and $\text{sign}(\bar H)$ is the sign of $\bar H$.

One can see that the total shrinkage coefficient k (Equation 20) is stress dependent. That is why the associated deformation is called the stress-induced shrinkage. Furthermore, Equation 21 reveals that the total coefficient of thermal expansion $\bar{\alpha}$ is also stress dependent, as proposed already by Thelandersson [25, 26]. The corresponding increase of thermal deformation, termed the stress-induced thermal expansion, has been detected by some experiments [25, 26].

For three-dimensional generalization, one can apply the same derivation to the volumetric and deviatoric components separately, and then sum them up. One obtains

$$\Delta\varepsilon_{\text{sh},ij} = k_{ij}\,\Delta H, \qquad \Delta\varepsilon_{T,ij} = a_{ij}\,\Delta T \qquad (22)$$

in which

$$\left.\begin{array}{l} k_{ij} = k_{\text{sh}}[\delta_{ij} + (r\sigma_{ij} + r'\sigma^{\text{v}}\,\delta_{ij})\,\text{sign}(\bar{H})] \\ a_{ij} = a_{\text{T}}[\delta_{ij} + (\rho\sigma_{ij} + \rho'\sigma^{\text{v}}\,\delta_{ij})\,\text{sign}(\bar{H})] \end{array}\right\} \qquad (23)$$

where $\sigma^{\text{v}} = \sigma_{\text{kk}}/3$, δ_{ij} is the Kronecker delta, r and r' are constants for shrinkage, and ρ and ρ' are constants for thermal expansion.

Equations 22 and 23 for shrinkage and thermal expansion have been used in computations, along with k_{sh} from Equation 15.

3.4 Stress–strain relation for distributed microcracking

The microcracking that occurs in the tensile region of the cross-section under service loads has different characteristics from cracking and fracture under ultimate load. The microcrack density is quite low [9]. One has the so-called 'dilute' cracks, whose effect may be described in a continuum manner by a stress–strain relation. In the previous work, this was done by combining the uniaxial stress–strain relations for three principal directions in an isotropic model. The calculations for this paper have been performed with a different type of constitutive relation for dilute cracks, developed by Brockenbrough and Suresh [27], in which the microcracking damage is also assumed to preserve isotropy. Although this constitutive relation cannot be said to give distinctly more realistic results, it has a better theoretical foundation as it is to some extent based on the micromechanics of dilute microcracks. For the present problem, the stress–strain relations used by Bažant and Chern [6, 7] would nevertheless yield almost the same results.

As in some previous damage models, we will introduce the central idea that the elastic modulus of a micro-cracked material decreases gradually as the number of microcracks increases or the existing microcracks grow. For this purpose, different kinds of crack geometries and distributions have been analysed extensively, for example, randomly orientated penny-shaped cracks, elliptical cracks, slit cracks, aligned penny-shaped cracks, and aligned slit cracks [28, 29]. Based on those studies, the reduction of material stiffness can be expressed

approximately as a function of a single parameter, called the crack density β: $E/E_0 = v/v_0 = 1 - f_\beta(\beta)$, in which E_0 is the initial elastic modulus and v_0 is the initial Poisson's ratio. A linear approximation is found acceptable for $f_\beta(\beta)$

$$\frac{E}{E_0} = \frac{v}{v_0} = 1 - \frac{16}{9}\beta. \qquad (24)$$

Anyhow, the exact form of $f(\beta)$ can hardly be determined because the crack system inside concrete does not involve a single crack geometry and the aggregates, acting as inclusions, also exert influence. We use

$$\beta = \begin{cases} A_\beta\left(\dfrac{\bar{\sigma}}{\sigma_0} - 1\right)^{n_\beta} & |\bar{\sigma}| > \sigma_0 \\ 0 & \text{elsewhere} \end{cases} \qquad (25)$$

in which $\bar{\sigma} = (\sigma_1^2 + \sigma_2^2 + \sigma_3^2)^{1/2}$; A_β, n_β, and σ_0 are constants; and σ_β is a threshold stress for microcracking. A further parameter β_{s}, called the saturation crack density, has also been introduced in some models [27, 30].

To stimulate the irreversible deformation at unloading, an unloading parameter is introduced;

$$\lambda = 1 - \frac{\beta_{\text{u}}}{\beta_{\text{max}}} \qquad (26)$$

β_{u} is the closed crack density at unloading, and β_{max} is the maximum crack density attained before unloading. It is required that $0 < \lambda < 1$. Then the unloading secant modulus E_{u} is interpolated between E_0 and E_{min} (the elastic modulus at the start of unloading), and the same is done for Poisson's ratio

$$E_{\text{u}} = E_0\lambda + E_{\text{min}}(1 - \lambda), \quad v_{\text{u}} = v_0\lambda + v_{\text{min}}(1 - \lambda) \qquad (27)$$

The constitutive relations are

$$\sigma = C\varepsilon_{\text{s}} \qquad (28)$$

$$\dot{\sigma} = \dot{C}\varepsilon_{\text{s}} + C\dot{\varepsilon}_{\text{s}} = \frac{\partial C}{\partial E}\frac{\partial E}{\partial \beta}\frac{\partial \beta}{\partial t}\varepsilon_{\text{s}} + C\dot{\varepsilon}_{\text{s}} \qquad (29)$$

From Equations 24 and 25,

$$\frac{\partial E}{\partial \beta} = -\frac{16}{9}E_0 \qquad (30)$$

$$\frac{\partial \beta}{\partial t} = A_\beta n_\beta\left(\frac{\bar{\sigma}}{\sigma_0} - 1\right)^{n_\beta - 1}\frac{\sigma\cdot\dot{\sigma}}{\sigma_0\bar{\sigma}} \qquad (31)$$

Then the incremental stress–strain relation for elastic deformations with cracking (but excluding creep and shrinkage) is

$$\Delta\sigma = C(\Delta\varepsilon_{\text{s}} - \Delta\varepsilon_{\text{s}}'') \qquad (32)$$

with

$$\Delta\varepsilon_{\text{s}}'' = -C^{-1}\frac{\partial C}{\partial E}\frac{\partial E}{\partial \beta}\frac{\partial \beta}{\partial t}\varepsilon_{\text{s}} \qquad (33)$$

The unloading criterion is the sign of the increment of crack density $\Delta\beta$. $\Delta\beta < 0$ means that the crack density should decrease, which corresponds to unloading.

Equation 31 indicates that $\Delta\beta < 0$ is equivalent to $\sigma \cdot \Delta\sigma < 0$. At unloading, Equation 27 is used. For reloading ($\lambda > 0$ and $\Delta\beta > 0$), again Equation 27 is used.

3.5 Constitutive model for drying creep and comparison with test data

The experimental results shown in section 2 suggest that the deformations from each mechanism are additive. So the models for each mechanism may also be superposed to describe drying creep. Based upon such considerations, we use a series coupling model (Fig. 13). The basic creep is represented by a generalized Kelvin chain model, Equations 3–5. The free shrinkage and stress-induced shrinkage are from Equations 22 and 23; for a constant temperature field, the thermal strain vanishes; the microcracking model is from Equation 32. The total strain increment is

$$\Delta\varepsilon = \Delta\varepsilon_c + \Delta\varepsilon_s + \Delta\varepsilon_{sh} \tag{34}$$

where $\Delta\varepsilon_c$ is the strain increment representing the creep model, $\Delta\varepsilon_s$ is the strain increment due to microcracking, and $\Delta\varepsilon_{sh}$ is the strain increment representing shrinkage and stress-induced shrinkage:

$$\Delta\varepsilon_c = D_c^{-1}\,\Delta\sigma + \Delta\varepsilon_s'', \qquad \Delta\varepsilon_s = C^{-1}\,\Delta\sigma + \Delta\varepsilon_s'' \tag{35}$$

where D_c is the material stiffness matrix and $\Delta\varepsilon_c''$ are the inelastic strain increments [18]. By substituting Equations 35 and 22 into 34, we obtain the incremental constitutive relation for the total deformation:

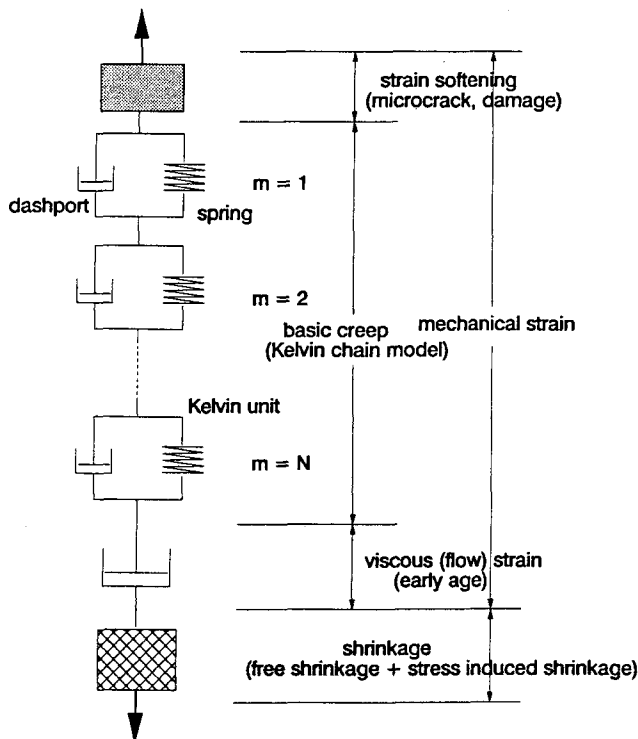$$\Delta\sigma = D(\Delta\varepsilon - \Delta\varepsilon'') \tag{36}$$

Fig. 13 Model for drying creep.

in which

$$D = (D_c^{-1} + C^{-1})^{-1} \tag{37}$$

$$\Delta\varepsilon'' = \Delta\varepsilon_c'' + \Delta\varepsilon_s'' + \Delta\varepsilon_{sh} \tag{38}$$

Before calibrating all the parameters in the model, it is helpful to analyse the effect of each parameter in order to reduce the number of parameters involved to the fewest possible.

First, in the model of basic creep, there are four parameters to be calibrated by tests, E_0 ($1/E_0 = q_1$), n, q_2, and q_3. Among these, q_3 can be neglected for the present purpose as long as the time ranges of the Kelvin units in the model cover the whole experimental duration; indeed, eight units are used in the present computations, with retardation halftimes ranging from 10^{-4} to 10^3. E_0 characterizes the asymptotic instantaneous deformation: Fig. 5 shows that the scatter of the instantaneous deformation is not large, and the computational results also indicate that the optimized E_0 will be slightly different for each deflection curve. Therefore, E_0 can be calculated by ACI approximate formula $E_0 = 57\,000\sqrt{f_c'}$ (with E_0 and f_c' in psi, 1 psi $\approx$ 6895 Pa), which gives quite good results. Thus, only n and q_2 need to be calibrated.

Second, in the shrinkage model there are three parameters, ε_s^0, r, and r'. Computational experience shows that $r' = 0$, that is, the mean stress has no effect on the stress-induced shrinkage. So, only two parameters, ε_s^0 and r, remain.

Finally, in the microcracking model, there are five parameters, A_β, n_β, σ_0, β_s, and λ. From Equation 24 one can see that $\beta_s < 9/16$ (otherwise E will decrease to 0); β_s is taken as 0.4 (same as references [27] and [30]). The experimental results show that the unloading stiffness is lower than E_0 but higher than the stiffness just before unloading. So, $\lambda = 0.5$ is used, which implies that E_u is the average of E_0 and E_{min}; n_β is the degree of nonlinearity as indicated in Equation 25, and $n_\beta = 0$ corresponds to linear elastic behaviour. A large value of n, say 10, results in elastic–plastic behaviour, and a smooth transition can be obtained by $n_\beta = 1.5$ according to the one-dimensional analysis of the model. Consequently, only two parameters, A_β and σ_0 are unknown. In total, 6 parameters remain to be found. Fortunately, they can be calibrated from the present test results sequentially.

The finite element mesh used is shown in Fig. 14. The finite elements were four-node quadrilaterals, 0.5 in by 0.5 in. The deformations for basic creep (sealed specimen, small eccentricity) are computed first and matched to the test results to identify the creep parameters n and q_2 (see Fig. 15). Then, the test data on basic creep plus stress-induced shrinkage (drying specimens, small eccentricity) are analysed to determine the shrinkage parameters ε_s^0 and r; the result is shown in Fig. 16, where the values of n and q_2 slightly differ from those in Fig. 15. Fig. 17 shows the deformed mesh of the drying specimen. Two-way spring elements are considered to be inserted in the interfaces between the end steel plate
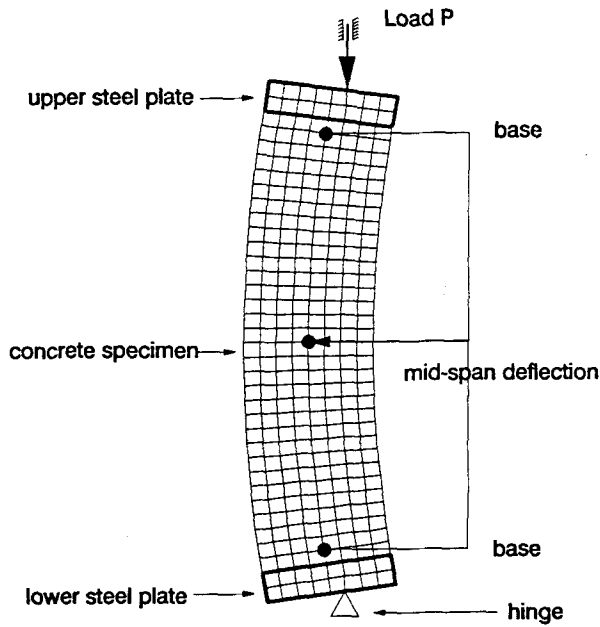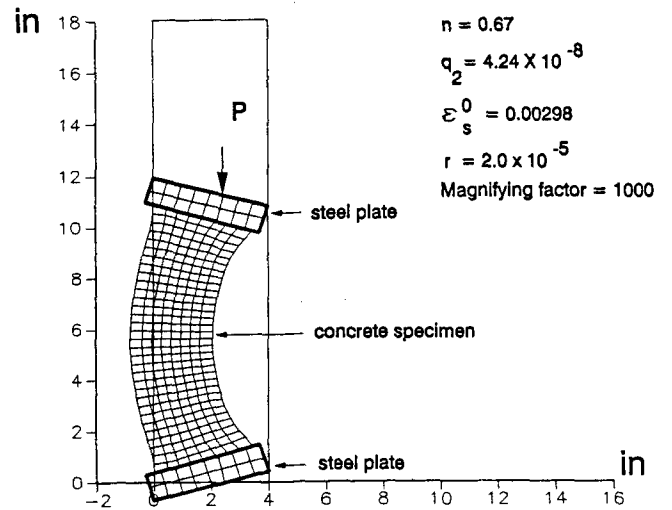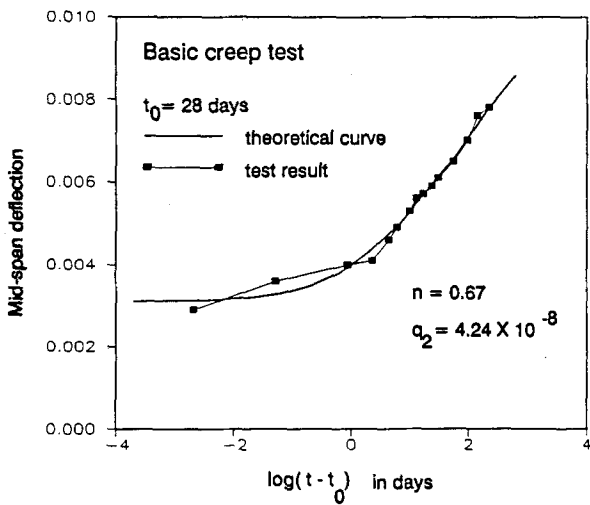
Fig. 14 Finite element mesh for analysis.

Fig. 15 Comparison with basic creep data.
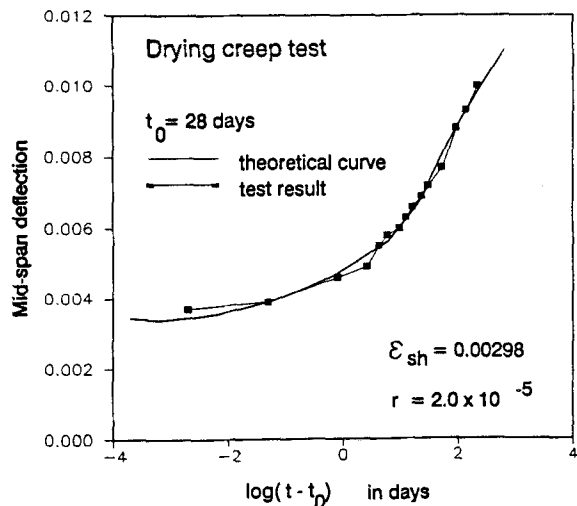
Fig. 16 Comparison with test data of basic creep and stress induced shrinkage.

Fig. 17 Deformed mesh for drying creep.

elements and the concrete elements, to allow the concrete elements to slide. Finally, the test data exhibiting all the mechanisms (drying specimens, large eccentricity) are analysed to evaluate parameters A_β and σ_0; the results are shown in Fig. 18.

In simulating the creep tests, the load is first increased from zero to the creep test level and then is held constant for the rest of the computation. For the drying specimens, the relative humidity profile is computed at each time step using the nonlinear diffusion model of Bažant, Xi and Molina [31]. The length of the time steps used for the nonlinear diffusion process is increased such that $t_{i+1}/t_i = 1.003$. The exponential algorithm is used for the time steps in the drying creep analysis. At each step, after the given convergence criterion is met, all of the internal variables are evaluated and stored for all stress components, at all integration points and all output points. The iterations at structure level are carried out according to the Newton–Raphson method. Thus, the strain increments accumulated during the iterations and the stress components in the previous time step need to be
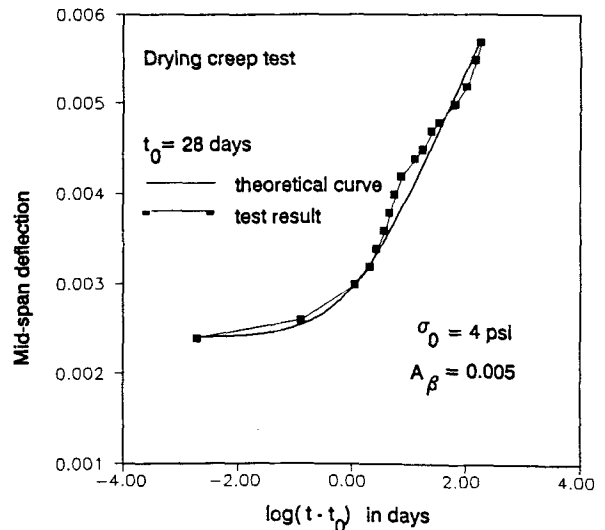

Fig. 18 Comparison with drying creep test data.

stored to be available for the iterations at the element level, because the viscoelastic creep increments and shrinkage strain increments are computed between two time steps.

To obtain the optimum values of the model parameters, a nonlinear optimization program (based on the Levenberg–Marquardt algorithm) is used. The nonlinear finite element program is arranged as a subroutine for this optimization program.

Figs 15, 16, and 18 indicate that the present model simulates drying creep behaviour well. The optimized values of the parameters for the present test results are given in the figures. In terms of the order of magnitudes, $n = 10^{-1}$, $q_2 = 10^{-8}$, $\varepsilon_s^0 = 10^{-3}$, $r = 10^{-5}$, $A_\beta = 10^{-3}$, and $\sigma_0 = 10^1$ psi. The orders of magnitude of these parameters are of more general interest than their precise values because, for different cement type, w/c, g/c, and s/c, the values of these parameters may change but not the order of magnitude (for example, ε_s^0 may vary from 0.0005 to 0.005).

4. CONCLUSIONS

1. A new experimental method, which allows direct separation of the components of drying creep due to microcracking and to stress-induced shrinkage, has been developed, demonstrated, and validated. The basic idea [16] is to compare the curvature creep of beams subjected to the same bending moment but very different axial forces. Such loading is achieved easily by applying axial forces of very different eccentricities and magnitudes.

2. Decomposition of the measured lateral deflections of eccentrically loaded prisms confirms the existence of the mechanism of stress-induced shrinkage. It follows that the deformations observed in drying creep tests result from four mechanisms: free shrinkage, basic creep (with elastic strain), stress-induced shrinkage, and microcracking.

3. The test results for different load levels indicate that the stress-induced shrinkage contributes to the total deformation at all load levels.

4. The stress-induced shrinkage monotonically increases with time. The microcracking effect increases at the beginning of drying, reaches a maximum (for the present specimen thickness) at about $t_m = 10$ days, and then it starts to decrease (the value of t_m may be expected to be approximately proportional to thickness squared).

5. It is possible and advantageous to use for the non-ageing viscoelastic constituent of concrete a continuous retardation spectrum associated with the Kelvin chain model.

6. A linear local constitutive relation between the relative humidity and the free (unrestrained) shrinkage strain of a material element is proposed and validated.

7. The coefficient of stress-induced shrinkage is derived on the basis of the microdiffusion theory for pore water. This coefficient reflects the fact that the associated viscosity is decreased by the microdiffusion process regardless of whether the microdiffusion transports water into or out of the gel pores.

8. The microcracking model of Brockenbrough and Suresh [27] is applied and is found to characterize nonlinear behaviour and irreversible deformation at unloading quite well.

9. To describe the drying creep tests, the models for basic creep, stress-induced shrinkage, and microcracking are coupled serially. The combined model characterizes each mechanism and the overall drying creep satisfactorily. Optimized model parameters are obtained, and the proper orders of magnitude of these parameters are given.

ACKNOWLEDGEMENTS

REFERENCES

1. Pickett, G., 'The effect of change in moisture content on the creep of concrete under a sustained load', *J. ACI* **38** (1942) 333–355.
2. Bažant, Z. P. and Wu, S. T., 'Creep and shrinkage law for concrete at variable humidity', *J. Engng Mech. ASCE* **100** (1974) 1183–1209.
3. Becker, J. and Bresler, B., 'Reinforced concrete frames in fire environments', *J. Struct. Div. ASCE* **103** (1977) 211–224.
4. Wittmann, F. H. and Roelfstra, P. E., 'Total deformation of loaded drying concrete', *Cem. Concr. Res.* **10** (1980) 601–610.
5. Iding, R. and Bresler, B., 'Prediction of shrinkage stresses and deformations in concrete', in 'Fundamental Research on Creep and Shrinkage of Concrete', edited by F. H. Wittmann (Martinus Nijhoff, 1982).
6. Bažant, Z. P. and Chern, J. C., 'Concrete creep at variable humidity: constitutive law and mechanism', *Mater. Struct.* **18**(103) (1985) 1–20.
7. Bažant, Z. P. and Chern, J. C., 'Strain-softening with creep and exponential algorithm', *J. Engng Mech. ASCE* **111**(3) (1985) 391–415.
8. Bažant, Z. P. and Chern, J. C., 'Stress-induced thermal and shrinkage strains in concrete', *Ibid*, **113**(10) (1987) 1493–1511.
9. Hwang, C. L. and Young, J. F., 'Drying shrinkage of Portland cement pastes, I, microcracking during drying', *Cem. Concr. Res.* **16** (1984) 584–594.
10. Bažant, Z. P. and Raftshol, W. J., 'Effect of cracking in drying and shrinkage specimens', *Ibid*, **12** (1982) 209–226.
11. Suzuki, K., Ohno, Y. and Ohra, H., 'Influence of the degree of restraint on cracking of concrete due to drying shrinkage', *Cem. Ass. Jap. Rev.* (1982) 145–147.
12. Beaudoin, J. J., 'Effect of humidity on subcritical crack growth in cement paste', *Cem. Concr. Res.* **15** (1985) 871–878.

13. Cohen, M. D., Olek, J. and Dolch, W. L., 'Mechanism of plastic shrinkage cracking in Portland cement and Portland cement–silica fume paste and mortar', *Ibid*, **20** (1990) 103–119.

14. Bažant, Z. P., 'Constitutive equation for concrete creep and shrinkage based on thermodynamics of multiphase systems', *Mater. Construct.* **3**(13) (1970) 3–36.

15. Bažant, Z. P., 'Thermodynamics of interacting continua with surfaces and creep analysis of concrete structures', *Nucl. Engng Design*, **20** (1972) 477–505.

16. Bažant, Z. P., 'Long-term modeling and prediction', Slide presentation at NSF Center for Advanced Cement-Based Materials, Center Industrial Affiliates Meeting, June 7 (Northwestern University, Evanston, IL, 1989); private communication by Y. Xi to S. G. Reid, Visiting Scholar at Northwestern University, June 1989.

17. Bažant, Z. P., Xi, Y. and Molina, L., 'Moisture diffusion in concrete and mechanisms of drying', in Proceedings of the ASCE Engng Mech. Specialty Conference (Columbus, OH, May 20–22, 1991) pp. 1146–1148.

18. Bažant, Z. P. and Xi, Y., 'New test method to separate microcracking from drying creep: curvature creep at equal bending moments and various axial forces', in Proceedings of the 5th International Symposium on Creep and Shrinkage of Concrete, edited by Z. P. Bažant and I. Carol (Chapman & Hall, London, 1993) pp. 77–82.

19. Bažant, Z. P., 'Mathematical Modeling of Creep and Shrinkage of Concrete' (John Wiley, New York, 1988).

20. Bažant, Z. P. and Xi, Y., 'Continuous retardation spectrum for solidification theory of concrete creep', *J. Engng Mech. ASCE* (1994) in press.

21. Bažant, Z. P. and Prasannan, S., 'Solidification theory of concrete creep, I, formulation', *Ibid*, **115**(8) (1989) 1691–1703.

22. Bažant, Z. P. and Prasannan, S., 'Solidification theory of concrete creep, II, verification and application', *Ibid*, **115**(8) (1989) 1704–1725.

23. Bažant, Z. P. and Cedolin, L., 'Stability of Structures: Elastic, Inelastic, Fracture, and Damage Theories' (Oxford, New York, 1991).

24. Bažant, Z. P. and Panula, L., 'Practical prediction of time-dependent deformation of concrete', *Mater. Struct.* Parts I and II, **11**(65) (1978) 307–328; Parts III and IV, **11**(66) (1978) 415–434; Parts V and VI, **12**(69) (1979) 169–183.

25. Thelandersson, S., 'On the multiaxial behavior of concrete exposed to high temperature', in Transactions of the 7th International Conference on Structural Mechanics in Reactor Technology (1983) Vol. H, H3/1.

26. Thelandersson, S., 'On the multiaxial behavior of concrete exposed to high temperature', *Nucl. Engng Design* **75** (1983) 271–282.

27. Brockenbrough, J. R. and Suresh, S., 'Constitutive behavior of a microcracking brittle solid in cyclic compression', *J. Mech. Phys. Solids*, **35**(6) (1987) 721–742.

28. Budiansky, B. and O'Connell, R. J. 'Elastic moduli of a cracked solid', *Int. J. Solids Struct.*, **12** (1976) 81–97.

29. Laws, N. and Brockenbrough, J. R., 'The effect of microcrack systems on the laws of stiffness of brittle solid', *Ibid.*, **23**(9) (1987) 1247–1268.

30. Evans, A. G. and Fu, Y., 'Some effects of microcracks on the mechanical properties of brittle solids – II, microcrack toughening', *Acta metall.*, **33**(8) (1985) (1525–1531).

31. Xi, Y., Bažant, Z. P., Molina, L. and Jennings, H., 'Moisture diffusion in cementitious materials: Moisture capacity and diffusivity', *J. Adv. Cement Based Mater.* (1994) in press.

32. Ali, I. and Kesler, C., 'Mechanisms of creep in concrete', ACI Special Publication SP-9, pp. 35–37 (American Concrete Institute, 1964).

RESUME

Fluage au séchage du béton: Modèle constitutif et nouveaux essais pour identifier ses mécanismes

On a développé, démontré et validé une nouvelle méthode expérimentale permettant d'identifier directement les composantes du fluage au séchage dû à la microfissuration et à la contrainte de retrait. L'idée de base est de comparer le fluage en flexion de poutres soumises au même moment fléchissant mais de faire varier les différentes forces axiales.

Les résultats confirment que le fluage au séchage a deux origines différentes: la microfissuration et le retrait sous contrainte. Celui-ci augmente de façon continue alors que celle-là augmente d'abord, puis diminue. On a utilisé un modèle d'élément fini pour ajuster les résultats d'essai qui valident le modèle actuel pour le fluage au séchage. On décrit la microfissuration par un modèle établi; quant au retrait libre (non empêché) d'un élément de matériau, on montre qu'il dépend de la chute d'humidité de façon approximativement linéaire.